ROYAL SOCIETY OF CHEMISTRY

PAPER

Check for updates

View Article Online
View Journal

Antibonding and electronic instabilities in GdRu₂X₂ (X = Si, Ge, and Sn): a new pathway toward developing centrosymmetric skyrmion materials

Dasuni N. Rathnaweera,[a] Xudong Huai,[a] K. Ramesh Kumar,[a] YiXu Wang,[b] Jane Schlesinger,[c] Christopher J. Bartel, [iD][c] Sumanta Tewari,[d] Michał J. Winiarski,[e] Richard Dronskowski [iD][b] and Thao T. Tran [iD] *[a]

Chemical bonding is key to unlocking the potential of magnetic materials for future information technology. Magnetic skyrmions are topologically protected nano-sized spin textures that can enable high-density, low-power spin-based electronics. Despite increasing interest in the discovery of new skyrmion hosts, the electronic origins of the skyrmion formation remain unknown. Here, we study $GdRu_2X_2$ (X = Si, Ge, and Sn) as a model system to investigate the connection between chemical bonding, electronic instability, and the critical temperature and magnetic field at which skyrmions emerge. The nature of the electronic structure of $GdRu_2X_2$ is characterized *via* chemical bonding, Fermi surface analysis, and the density of energy function. As X-p orbitals become more extended from Si-3p to Ge-4p and Sn-5p, improved interactions between the Gd spins and the $[Ru_2X_2]$ conduction layer, along with increased destabilizing energy contributions, are obtained. $GdRu_2Si_2$ possesses a Fermi surface nesting (FSN) vector $[\boldsymbol{Q} = (q, 0, 0)]$ r.l.u.; whereas $GdRu_2Ge_2$ displays two inequivalent FSN vectors $[\boldsymbol{Q}_A = (q, 0, 0); \boldsymbol{Q}_B = (q, q, 0)]$ r.l.u., and $GdRu_2Sn_2$ features multiple $\boldsymbol{Q}$ vectors. In addition, competing ferromagnetic and antiferromagnetic exchange interactions in the Gd plane become more pronounced as a function of X. These results reveal a correlation among the electronic instability, the strength of competing magnetic interactions, and the temperature and magnetic field conditions under which skyrmions form. This work demonstrates how chemical bonding and electronic structure can enable a new framework for understanding and developing skyrmions under desired conditions that would otherwise be impossible.

1. Introduction

Understanding how chemical bonding and electronic instability influence magnetic phase transitions is crucial for developing materials for various applications, including spintronics, sensors, and quantum technologies.[1–10] Skyrmions are dynamic, particle-like magnetic states capable of twisting and turning in a unique way, with sizes ranging from a few nanometers to ∼100 nm, and exhibit unique properties arising from their non-trivial topology. Their topologically protected properties provide a promising platform for studying the interaction between electronic effects and magnetic phase transitions while improving our understanding of novel states of matter.[11–18] Topological protection enables skyrmions to maintain their unique properties even in the presence of defects in real materials, offering new opportunities for developing next-generation information carriers and memory architectures.[19–21]

Skyrmion evolution in noncentrosymmetric magnets is driven by antisymmetric Dzyaloshinskii–Moriya interactions,[22–33] whereas skyrmion formation in centrosymmetric magnetic metals is facilitated by a delicate balance between competing exchange interactions, the Ruderman–Kittel–Kasuya–Yosida (RKKY) interactions, frustrated exchange coupling, and dipolar interactions. The long-range RKKY exchange interaction $J(r) \sim \sin(2k_F r)/r^3$, where k_F is the Fermi wavevector of conduction electrons, and r is the distance between the magnetic moments,

[a] *Department of Chemistry, Clemson University, Clemson, South Carolina, 29634, USA. E-mail: thao@clemson.edu*

[b] *Chair of Solid-State and Quantum Chemistry, Institute of Inorganic Chemistry, RWTH Aachen University, 52056, Aachen, Germany*

[c] *Department of Chemical Engineering and Materials Science, University of Minnesota, Minneapolis, Minnesota, 55455, USA*

[d] *Department of Physics, Clemson University, Clemson, South Carolina, 29634, USA*

[e] *Faculty of Applied Physics and Mathematics and Advanced Materials Center, Gdansk University of Technology, ul. Narutowicza 11/12, 80-233, Gdansk, Poland*
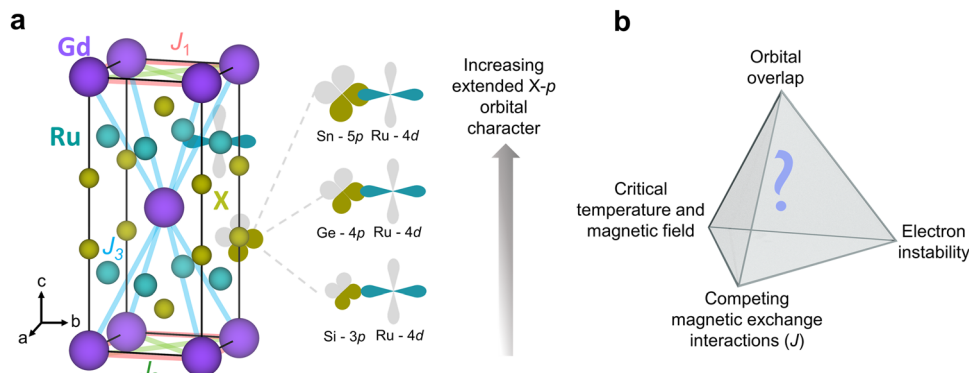
Fig. 1 (a) Crystal structure of $GdRu_2X_2$ (X = Si, Ge, and Sn) showing exchange interactions and increased dispersion of X-p orbitals going from Si-3p to Ge-4p and Sn-5p, and (b) potential connections among orbital overlap, electron instability, and competing exchange interactions, and critical temperature and magnetic field conditions at which skyrmions emerge.
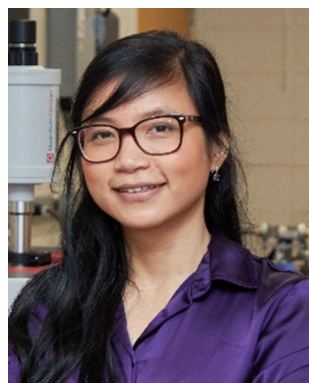
assisted by intra-orbital magnetic frustration, promotes the formation of skyrmions with small sizes (a few nm).[13,34–39]

Gd-based centrosymmetric tetragonal lattice systems, $GdRu_2X_2$ (Gd^{3+}, $S = 7/2$, $L = 0$, X = Si and Ge), have been demonstrated as skyrmion hosts with rich magnetic phase diagrams.[40–44] This is in part attributable to the unique crystal structure and chemical flexibility, allowing an array of atomic substitutions (Fig. 1a). Recent theoretical studies on skyrmion hosts adopting centrosymmetric tetragonal lattices suggested several microscopic origins for skyrmion emergence, such as RKKY exchange interactions, and interorbital frustration originating in Gd-d–f spins can stabilize a spin structure with a finite modulation vector, Q.[45] Magnetic frustration, anisotropy, high-order spin interactions and FSN have been recognized as essential physical parameters to induce phase transitions to skyrmions at a given field and temperature.[46,47] The elegant studies provided valuable insights into the microscopic origins of centrosymmetric skyrmion materials; however, chemical

Thao Tran is a Dean's Associate Professor in Chemistry at Clemson University. She received her PhD from the University of Houston and conducted postdoctoral research at Johns Hopkins University and the Institute for Quantum Matter. Her research team studies materials chemistry, focusing on how electronic structure and fundamental physical principles can be harnessed to address key challenges in quantum information science and energy technologies. Her research program has been supported and recognized by multiple federal and private foundations. Her students and postdoctoral researchers have received numerous awards, and her former team members are now thriving in industry, national laboratories, and academia.

Thao T. Tran

connections to critical temperature and magnetic field conditions at which skyrmions emerge remain elusive. This significantly hinders the materials development of skyrmions that may evolve at room temperature and zero field.

It has been demonstrated that in $GdRu_2Si_2$, indirect RKKY interactions stabilize equivalent magnetic modulation vectors, resulting in a square skyrmion lattice at 2 T $\leq \mu_0H \leq$ 2.5 T, 2 K $\leq$ T $\leq$ 20 K, with the smallest diameter of 1.9 nm among the known skyrmion materials.[42,48,49] Magnetic torque and resistivity measurements revealed that FSN enhances the strength of the RKKY interaction, resulting in a helical modulation Q_A = (0.22, 0, 0) r.l.u. in $GdRu_2Si_2$.[42,50] Angle-resolved photoelectron spectroscopy measurements in conjunction with density functional theory calculations revealed a nested Fermi surface (FS) band at the corner of the Brillouin zone that is responsible for the skyrmion formation in the Si material.[51] $GdRu_2Ge_2$—an isostructural compound—has recently been realized to feature the successive formation of two distinct skyrmion pockets.[40,41] Resonant X-ray scattering and magneto-transport studies suggested the presence of competing RKKY exchange interactions at inequivalent wavevectors, [Q_A = (q, 0, 0) r.l.u. and Q_B = ($q/2$, $q/2$, 0) r.l.u.] that drive such rich topological phase formation.[40] Our previous studies have demonstrated the evolution of two skyrmion pockets in $GdRu_2Ge_2$ at 2 K $\leq T \leq$ 30 K, 0.9 T $\leq \mu_0H \leq$ 1.2 T and 1.3 T $\leq \mu_0H \leq$ 1.7 T. It is worth noting that the skyrmions in $GdRu_2Ge_2$ form at higher temperatures and lower fields than those in $GdRu_2Si_2$. Electronic structure and exchange interaction evaluations revealed that the more extended Ge-4p orbitals, compared to Si-3p, enhance competing exchange interactions, thereby making the phase transition to skyrmions more accessible in $GdRu_2Ge_2$ (at higher temperatures and lower fields).[41]

This work provides a systematic investigation of how electronic structure and chemical bonding manifest the temperature and magnetic field conditions for skyrmion evolution in the isostructural model system $GdRu_2X_2$ (X = Si, Ge, and Sn). While the Sn compound has not been experimentally realized due to its thermodynamically unfavorable formation energy (Fig. S1a and b), its hypothesized crystal structure is optimized for this study using

variable cell calculations. Our research goal is to provide some answers to the central scientific questions: What are the underlying chemical and electronic parameters that influence the formation of skyrmions in $GdRu_2X_2$? How do they manifest in critical temperature and magnetic field conditions at which skyrmions emerge? (Fig. 1b). In this study, we employ density functional theory (DFT) calculations to investigate chemical bonding *via* crystal orbital Hamilton population (COHP) and crystal orbital bond index (COBI), analyze Fermi surface nesting, probe electronic instability through the density of energy (DOE), and use total-energy methods to elucidate the exchange interactions in the model system. This approach enables us to delve into the impact of Si-3p/Ge-4p/Sn-5p on the orbital overlap and electronic structure of $GdRu_2X_2$ and connect the chemical bonding concepts to skyrmion formation.

2. Computational details

2.1 Quantum ESPRESSO DFT calculations

The spin-polarized electronic structure, density of states, and Fermi surface calculations were performed using the Quantum ESPRESSO (QE) package. A kinetic energy cutoff of 60 Ry for the plane-wave basis set and 452 Ry for the charge density was used. The interaction between core and valence electrons was described using the projector augmented-wave (PAW) method, and the exchange–correlation functional was treated within the Perdew–Burke–Ernzerhof (PBE) formulation. For Gd, the valence configuration included $4f^7$, $5d^1$, $6s^2$ with semicore $5s^2$, $5p^6$. For Ru, the valence configuration consisted of $4d^7$, $5s^1$ with semicore $4s^2$, $4p^6$. For Ge, the valence configuration included $4s^2$, $4p^2$, and semicore $3d^{10}$. The on-site Coulomb interaction (Hubbard parameter) and Hund's exchange parameter for the Gd-4f level were set to be $U = 6.7$ eV and $J = 0.7$ eV. The double-counting correction was handled by the fully localized limit (FLL) double-counting scheme, as implemented in QE. The Brillouin zone integrations were performed using a $13 \times 13 \times 6$ Monkhorst–Pack k-point mesh to achieve self-consistency of the energy threshold of 5×10^{-9} Ry. Lattice parameters for $GdRu_2Sn_2$ were estimated using variable cell calculation. The pseudopotential DFT calculations for the J-coupling constant used the same parameter, except that the k-mesh was changed to $3 \times 3 \times 2$ to account for the $(2a, 2b, c)$ super cell. The charge and spin density maps are calculated using pp.x in the QE package and visualized using the VESTA software. The pseudo-potential wavefunctions calculated from the QE package are projected into a linear combination of atomic orbitals (LCAO) based representation by means of the local orbital basis suite towards the electronic-structure reconstruction (LOBSTER)[52] program to extract the projected COHP (pCOHP),[53] k-space COHP,[54] COBI,[55] DOE[56] and the molecular orbital diagrams. k-Space COHP data were visualized using the functionalities implemented within the LOPOSTER code.[57]

Additional SCF calculations were performed to compute the Lindhard response function (LRF). To extract the Fermi surface, the self-consistent field (SCF) calculation was performed using a denser Monkhorst–Pack (MP) k-point grid. The Brillouin zone

was numerically integrated for the total energy estimation using a $38 \times 38 \times 19$ MP k-point sampling. The Fermi velocity across the Brillouin zone was mapped onto the Fermi surface as a color plot. The orbital character of the Fermi surface was computed using the Fermi projector operator, which calculates the following quantity: $\sum_{i=1}^{n_s} \left| \phi_{n_{s(i)}}^{atom} | \phi_{nk} \right|^2$ where n_s represents the number of target wavefunctions. The results from this Fermi projection calculation are saved in a format compatible with the FermiSurfer 2.4.0 software for visualization.[58]

2.2 Green's function-based DFT calculations

To estimate the magnetic exchange constants (J_{ij}), the Dzyaloshinskii–Moriya interactions (D_{ij}), and the magnetocrystalline anisotropy constant (K), we employed the Green's function and multiple scattering theory based DFT calculations using the spin-polarized relativistic Korringa–Kohn–Rostoker (SPR-KKR) code.[59] The exchange–correlation potential was treated within the local density approximation (LDA) using the Vosko–Wilk–Nusair (VWN) parameterization.[60] Self-consistent field (SCF) calculations were carried out using the spin-polarized scalar-relativistic (SP-SREL) Dirac Hamiltonian. To achieve self-consistency, the Brillouin zone integration was carried out using a $41 \times 41 \times 41$ k-mesh, corresponding to 68 921 k-points in the full Brillouin zone, equivalent to 4851 irreducible k-points. The SCF mixing parameter, energy convergence tolerance and the angular momentum cutoff were set to 0.2, 0.01 mRy, respectively. The above SCF conditions successfully converged the potential, and all subsequent post-processing calculations were carried out using this converged potential. Magnetic exchange constants J_{ij} were computed within the magnetic force theorem using the Liechtenstein–Katsnelson–Antropov–Gubanov (LKAG) scheme.[61] Real-space couplings were evaluated up to a cluster radius $R_c = 7.0$ and the reciprocal space coupling constants $J(q)$ were obtained by performing a lattice Fourier transform. For estimating the Dzyaloshinskii–Moriya interactions (D_{ij}) and the magnetocrystalline anisotropy energy (MAE), we carried out fully relativistic (REL) calculations using the same SCF parameters as in the scalar-relativistic calculations.

3. Results and discussion

3.1 Electronic structure

We have previously studied the skyrmion host $GdRu_2Ge_2$, which adopts a $ThCr_2Si_2$-type structure—with a centrosymmetric tetragonal space group $I4/mmm$.[41] For the magnetoentropy mapping, electrical transport and heat capacity data of the Ge material, the reader is invited to visit the reference.[41] The previous results laid some groundwork for our systematic studies on the isostructural centrosymmetric magnets $GdRu_2X_2$ (X = Si, Ge, and Sn), of which the structure includes the Gd square lattice connected to $[Ru_2X_2]$ layers (Fig. 1a). To gain insight into how the electronic structure of $GdRu_2X_2$ determines its physical properties, pseudo-potential spin-polarized DFT calculations were performed using the QE software package.[62] The crystal structure information of

GdRu$_2$X$_2$ used in the DFT computations is provided in Table S1. The band structure and density of states (DOS) results clearly demonstrate some common electronic features in GdRu$_2$X$_2$ (Fig. 2). The spins of the Gd-4f states are polarized, which then polarizes the Ru-4d and X-p states. The contribution of Gd-4f states is localized, deep in low energy ~ -8 eV for majority spins, and slightly above the Fermi level (E_F) energy ~ 4 eV for minority spins. The spin-polarized band structure and density of states of GdRu$_2$X$_2$ display a metallic behavior, where multiple bands cross E_F and finite DOS at E_F. These features demonstrate that interactions between the localized Gd-4f magnetic moments are mediated by itinerant electrons through RKKY interactions. Around E_F, the bands are mostly comprised of the Gd-5d, Ru-4d, and X-p states. The band structures exhibit an increase in overall band dispersion as the valence electron configurations progress from Si-3p, Ge-4p, and Sn-5p. This distinction becomes clearer when examining the derivatives

dE/dk and d^2E/dk^2 of the bands that are crossing the Fermi level. Among the 5 bands, particularly in Band-2 near the Z point, Si bands display a sudden change in slope, which gives the appearance of an abrupt dispersion change (Fig. S10). By contrast, the corresponding bands for Ge and Sn evolve more smoothly and exhibit nearly parabolic dispersion, indicating more dispersive features. As a result, the extended X-p orbital character generates more diffuse features in Gd-d and Ru-d orbitals, improving the interaction between Gd–X and Ru–X (Fig. 2).

3.2 Chemical bonding analysis

DOS analysis is helpful in describing the atom projected state contribution; however, it does not capture the phase relationships among the orbitals involved in the overlapping wavefunctions. To extract the information on bonding characters (bonding = constructive interference of wavefunctions, nonbonding = zero
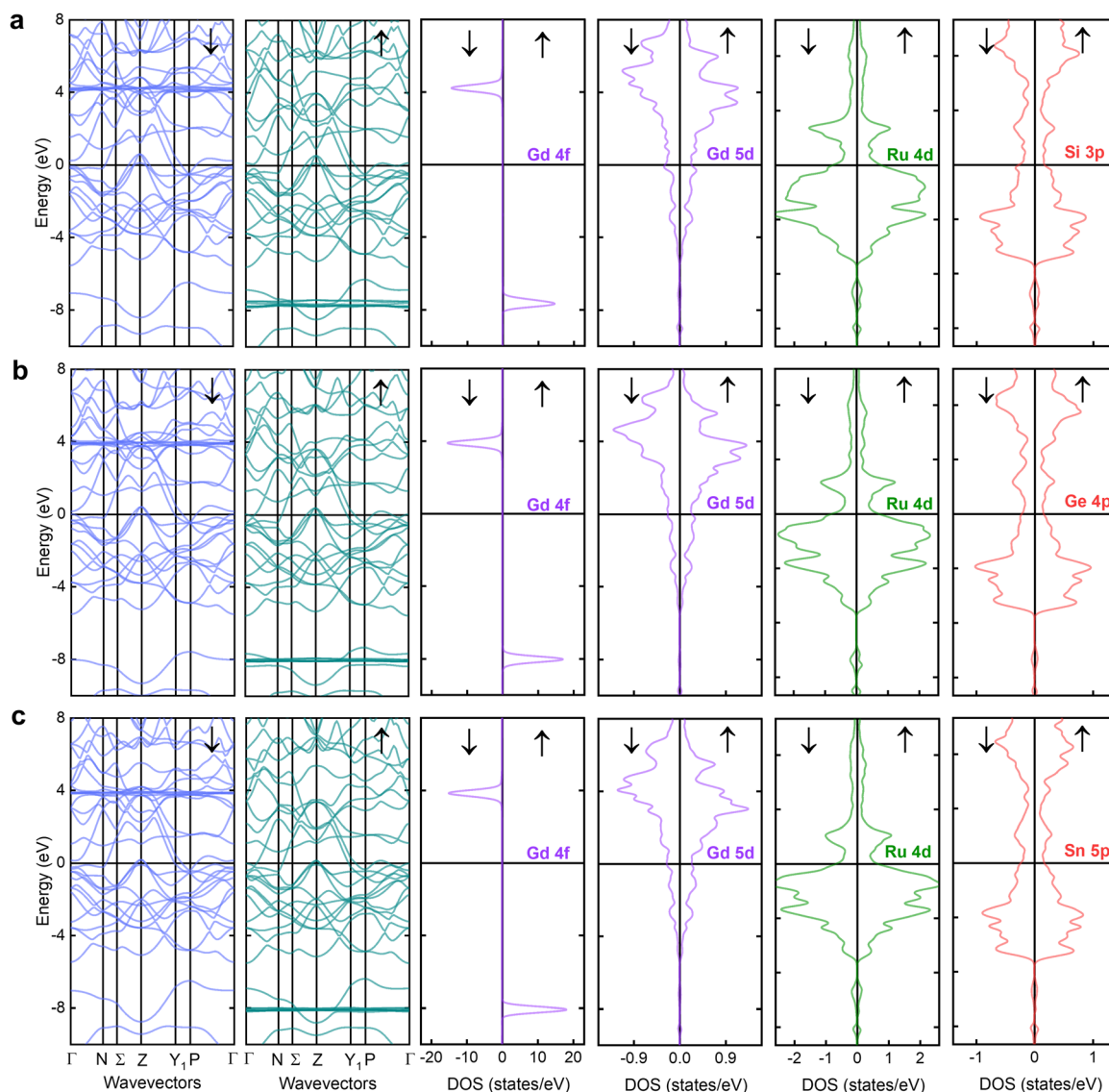

Fig. 2 Spin-polarized band structures showing bands around the Fermi level and spin-polarized DOS of (a) GdRu$_2$Si$_2$, (b) GdRu$_2$Ge$_2$, and (c) GdRu$_2$Sn$_2$.

interference, and antibonding = destructive interference) and how the microscopic mechanisms can influence skyrmion formation, we used the local orbital basis suite towards electronic-structure reconstruction (LOBSTER) program to reconstruct the local-orbital picture from PAW wavefunctions.[63–67]

Crystal orbital Hamilton population (COHP) determines the energy-resolved bonding, antibonding, or nonbonding contributions between interatomic (pair-wise) interactions; whereas integrated COHP (ICOHP) estimates the overall strength of a chemical bond.[53,65] The projected COHP (pCOHP) curves (Fig. 3)

indicate bonding character ($-$pCOHP > 0) for Gd–Gd, Gd–X, and X–X bonds and antibonding character ($-$pCOHP < 0) for Ru–Ru and Ru–X bonds around E_F. The integrated COHP (ICOHP) value of Gd–Gd decreases as X changes from Si to Ge and Sn, suggesting a reduced overlap of the Gd orbitals. For the [Ru_2X_2] conduction layer, the increased ICOHP value of Ru–X implies an improved overlap of the Ru-d and X-p orbitals as X changes from Si to Ge and Sn. These combined features provide some insight into the improved interaction between the Gd-4f localized electrons and the [Ru_2X_2] layer as X changes from Si to Ge and Sn.
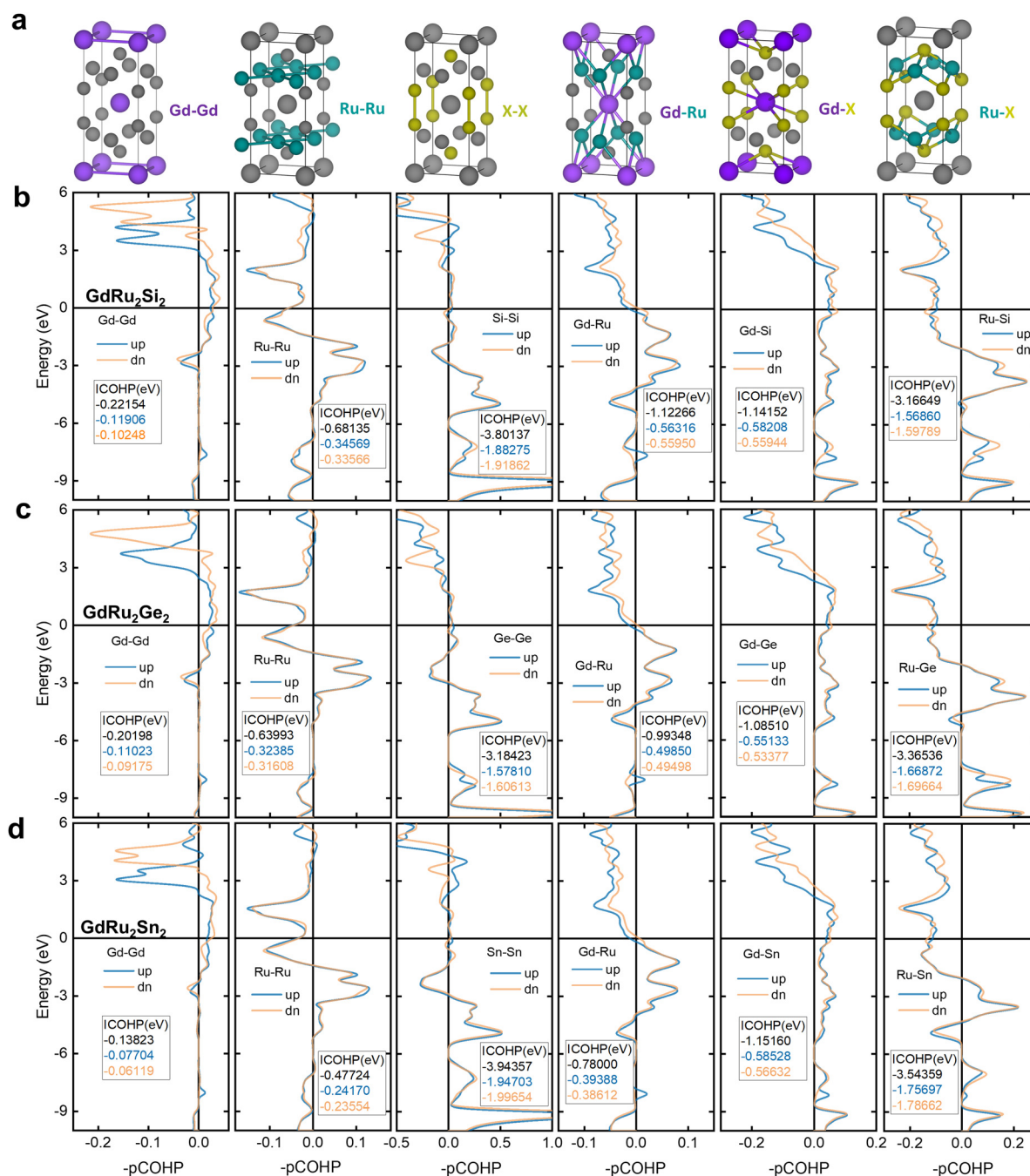

Fig. 3 Projected crystal orbital Hamilton population ($-$pCOHP) curves for (a) relevant bonding environments, (b) GdRu$_2$Si$_2$, (c) GdRu$_2$Ge$_2$, and (d) GdRu$_2$Sn$_2$ with their integrated values (ICOHP).

The crystal orbital bond index (COBI) provides a generalized bond index term for crystalline solids. To quantitatively analyze the quantum-chemical bond order in solids, the integrated COBI (ICOBI)[55,68] was calculated for all bonds (Fig. S3). Ru–X and X–X bonds have the greatest ICOBI values of ~ 0.5, about half a bond, indicating a strong covalent bonding character. The small ICOBI value of Gd–Gd (~ 0.03) implies negligible pairwise interactions. Overall, the COBI results are in line with and complementary to the COHP.

To gain more insight into the anti-bonding occupation around the E_F, we calculated the k-resolved COHP for Ru-4d and X-p bonds in GdRu$_2$X$_2$, since these orbitals are the main composition of the E_F.[69] The k-COHP maps (Fig. 4) reveal that the bonding sign switches to antibonding well below E_F and then persists up to and across E_F, with a continuous antibonding range from roughly -1.2 eV to 0 eV, for both Ru–X and Ru–Ru pairs. Moving from Si to Ge and Sn, the Ru–X antibonding strengthens modestly (Fig. 4, first two rows), whereas the Ru–Ru antibonding grows substantially (Fig. 4, last two rows), indicating that the common Ru sublattice experiences progressively stronger destabilization around E_F as a function of X. We attribute this trend to strong bonding among [Ru$_2$X$_2$] slab (seen in the COHP) that enhances Ru–X mixing and, in turn, feeds the Ru–Ru antibonding near E_F. Spin-resolved panels show nearly comparable contributions from the majority and minority spins, with the minority spin channel lying slightly closer to E_F; thus, the effect is not strongly spin-selective in this collinear setting.

Crucially, the strongest, flat, antibonding segments near E_F cluster along Γ–X and P–N in the -1.2 eV to 0 eV energy window, while X–P also appears antibonding but sits relatively farther from E_F (Fig. 4). This directional pattern matters: the Γ–X and P–N segments identify the k-space regions most capable of low-energy scattering, providing a bond-specific map of where the electronic structure is primed for modulation. Along P–N, the k-COHP plot shows a progressive shift of antibonding bands toward E_F: it remains below E_F in Si, approaches E_F in Ge, and crosses E_F in Sn. Together with the flat, near-E_F antibonding seen along Γ–X, these features delineate specific k-space segments where low-energy scattering is available. While a full analysis is presented later, we note that this evolution could be consistent with the directions of the FSN vectors and may relate to the multi-Q behavior observed only in Ge and Sn compounds.

3.3 Spin density analysis

Spin, charge, and orbital are the three fundamental components of an electron. Next, we examine spin and charge density maps while considering orbital contributions. Spin density maps ($\rho_{up} - \rho_{down}$) projected on selected lattice planes illustrate supplementary evidence for the effect of the X-p orbitals on spin polarization (Fig. 5).[70] In the [100] plane cutting through Gd, Ru, and X (Fig. 5a), the spin polarization of the [Ru$_2$X$_2$] layer is enhanced as X changes from Si to Ge and Sn. Fig. 5b and c show the [001] plane slicing through Gd and X and between Ru and X, respectively. The spin density of Gd and Ru in these projections becomes more polarized, following the

trend GdRu$_2$Si$_2$ < GdRu$_2$Ge$_2$ < GdRu$_2$Sn$_2$. The tunable spin polarization as a function of X-3p/4p/5p orbitals suggests the feasibility of modifying interactions between the Gd localized magnetic spins and the [Ru$_2$X$_2$] conduction layer-ingredients for RKKY interactions. As shown in Fig. 5a–d, the Gd site exhibits a strong, red-colored, spherically symmetric contour pattern, indicating well-localized Gd-4f magnetic moments. In the vicinity of the Gd moment, the Ru–X layer exhibits spin density in the blue-purple color, reflecting strong hybridization between the Ru-4d states and X-p states (Fig. 5a). If we interpret the blue-purple region as induced spin polarization due to the RKKY interaction, it becomes evident from Fig. 5a that the substitution of the X atom from Si to Ge to Sn leads to subtle changes in both the intensity and the spin density contours along the [100] direction. The contour lines emerging along the [100] projection indicate spin density elongation and are associated with the FSN vector $Q_A = (q, 0, 0)$ r.l.u. experimentally observed for GdRu$_2$Si$_2$ and GdRu$_2$Ge$_2$.[40,42] Additionally, short, wave-like modulations in the form of spin density lobes along the b-axis are observed in Fig. 5a. The spin density wave along the a-axis (a and b are equivalent in tetragonal systems) can be linked to the experimentally observed propagation vector $Q_A = (0.22, 0, 0)$ r.l.u. Furthermore, the Ge variant shows visibly stronger polarization and a tendency to diffuse along the c-axis, suggesting that the enhanced orbital spatial extension of Ge-4p and Sn-5p facilitates increased hybridization and thereby supports FSN. Another interesting feature is observed along the [110] direction in the spin density contours. For the Si system, we observe nearly isotropic spin polarization at the Gd site. In contrast, the Ge and Sn variants exhibit reconfigured spin density contours around Gd, indicating the presence of additional spin density modulations (Fig. 5d). This observation aligns with experimental reports of inequivalent multiple modulation vectors in GdRu$_2$Ge$_2$. Since we do not observe a clear antiferromagnetic-like coupling between the 4f moments and the Ru–X layer as seen in the [100] modulation, the spin density contours along [110] may originate from inter-orbital frustration between Gd-4f and Gd-5d. Similar spin density features are observed in the [110] projection (Fig. S5), connecting to the $Q_B = (q, q, 0)$ r.l.u. FSN vector in GdRu$_2$X$_2$. A more detailed description of FSN is discussed in the subsequent sections.

3.4 Charge density analysis

In addition to the spin density, charge density maps visually represent the distribution of electronic charge within the GdRu$_2$X$_2$ crystal (Fig. 6).[70] Fig. 6a highlights the [110] projection on the Gd and X planes. As X changes from Si to Ge to Sn, the charge density of the X–X dumbbells increases, enhancing the charge anisotropy of Gd. Meanwhile, Fig. 6b shows the [110] plane cutting through the Ru layer, where the charge distribution of Gd appears more diffused. Fig. 6c and d show the [001] projections on the Gd and X plane and the plane between Ru and X, respectively. As X goes from Si to Ge and Sn, the charge density of Gd and [Ru$_2$X$_2$] increases and becomes more dispersed. This indicates improved bonding interactions between Gd and [Ru$_2$X$_2$].
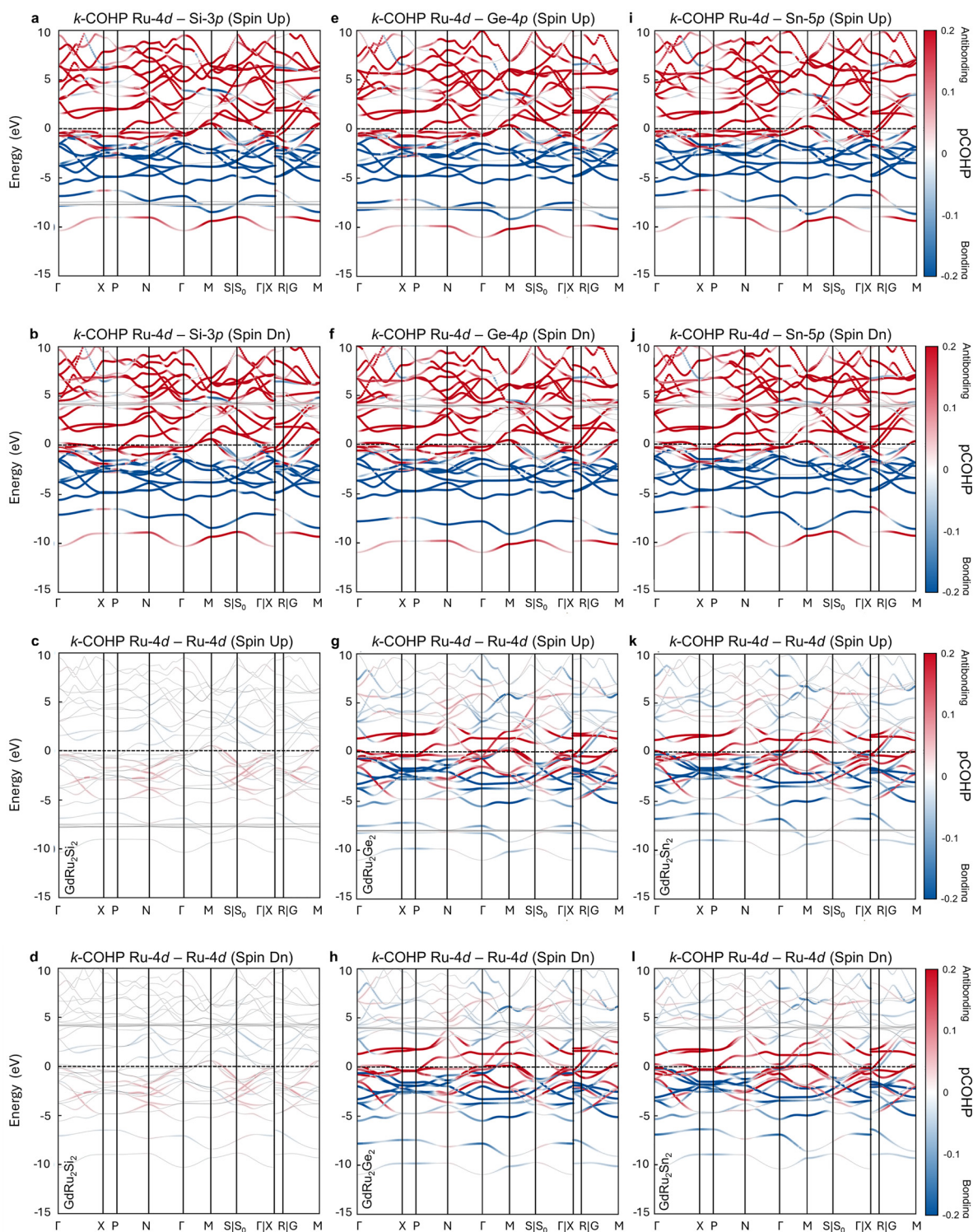
Fig. 4 k-resolved COHP of Ru–X and Ru–Ru near E_F along the Γ–X–P–N–Γ–M path for (a–d) GdRu$_2$Si$_2$, (e–h) GdRu$_2$Ge$_2$, (i–l) GdRu$_2$Sn$_2$. The color scale represents pCOHP (eV).

3.5 Electronic instability

3.5.1 Fermi surface nesting and Lindhard response function.
Electronic instability around E_F in metals gives rise to phase transitions to novel states of matter under external perturbations, such as temperature and field.[69,70] To describe how itinerant electrons behave under the influence of various interactions in GdRu$_2$X$_2$, we extracted the Fermi surface from the bands that cross E_F. The Fermi surface topology and potential nesting in the
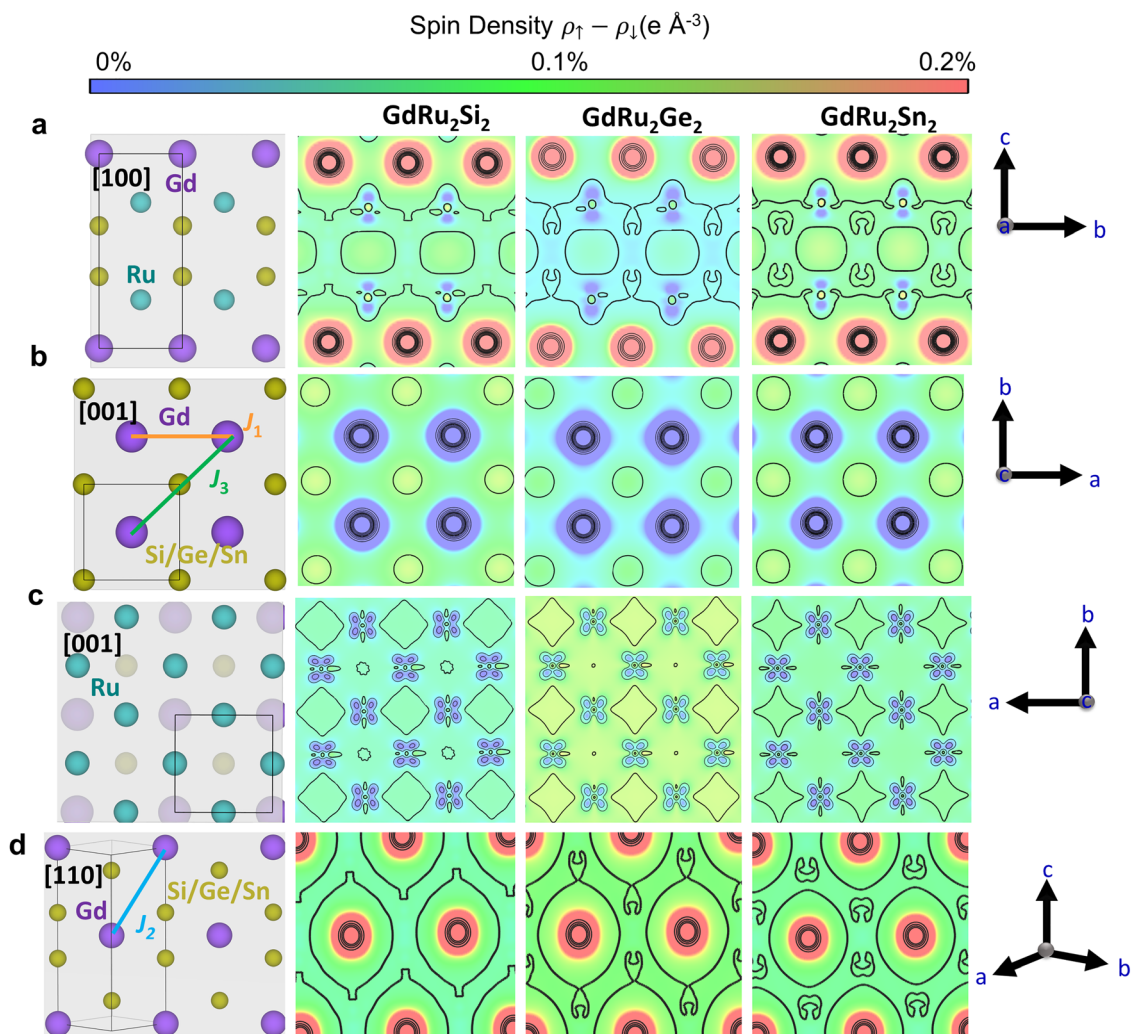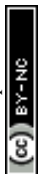
Fig. 5 Spin density map of GdRu$_2$X$_2$ (a) [100] plane cutting through Gd, Ru, and X atoms, (b) [001] plane cutting though Gd and X atoms, (c) [001] plane cutting in between Ru and X atoms, and (d) [110] plane cutting through Gd atoms (X = Si, Ge, and Sn). The color bar provides a qualitative indication of the relative magnitude of spin polarization.

Si and Ge materials as well as in Gd$_2$PdSi$_3$ have been realized to enable spin spiral magnetic ordering and double-Q density wave modulation.[40,46,51,71] There are situations where sections of the Fermi surface are parallel (or nearly parallel) and can be connected by a single nesting vector Q, leading to instabilities such as charge and spin density waves in materials. There is a general agreement in the literature regarding the FSN driving the helical and skyrmion phases. However, minor discrepancies arise regarding the specific nesting vector. Despite several studies, the precise modulation vector and the specific portion of the FS responsible for nesting remain unresolved in GdRu$_2$X$_2$ (X = Si and Ge).

To further understand FSN in GdRu$_2$X$_2$ (X = Si, Ge, and Sn) and whether and how the modification of X-p orbitals influences nesting vectors, we examine the FS and the LRF for GdRu$_2$X$_2$. Fig. 7 and 8 present the FS diagrams for both spin-up and spin-down channels, along with the corresponding LRF projected along the [100] and [111] directions, respectively. Our calculations showed five distinct FSs in the Si and Ge materials, and only four FSs in the Sn variant (Fig. S6), agreeing well with

the band structures. The presence of small, ellipsoidal FSs at the Z point is common in GdRu$_2$X$_2$ (Fig. S6). These smaller ellipsoid pockets are identified as localized hole pockets and show parallel features at the Z point. However, LRF and other experimental evidence are absent for such modulation. A larger barrel-like FS (band 4 for Si/Ge and band 3 for Sn) is observed in all three compounds. This surface extends to the zone boundary and shows strong dispersion along the k_x and k_y directions with limited dispersion along the k_z direction (Fig. S6). These features are observed for both spin-up and spin-down channels. Additionally, band 5 (band 4 for Sn) shows a distinct difference between spin-up and spin-down channels. We observed a less dispersive parallel surface centered at the X point in the spin-down channel. In contrast, the spin-up band is well extended (tubular type FS) within the Brillouin zone, suggesting significant band interaction, possibly due to the influence of 4f and 5d orbital mixing and/or multi-band effects of Ru-4d (Fig. 7a, c and e). This band primarily arises from Gd-5d and Ru-4d states, crosses E_F at multiple k-points, and displays linear dispersion
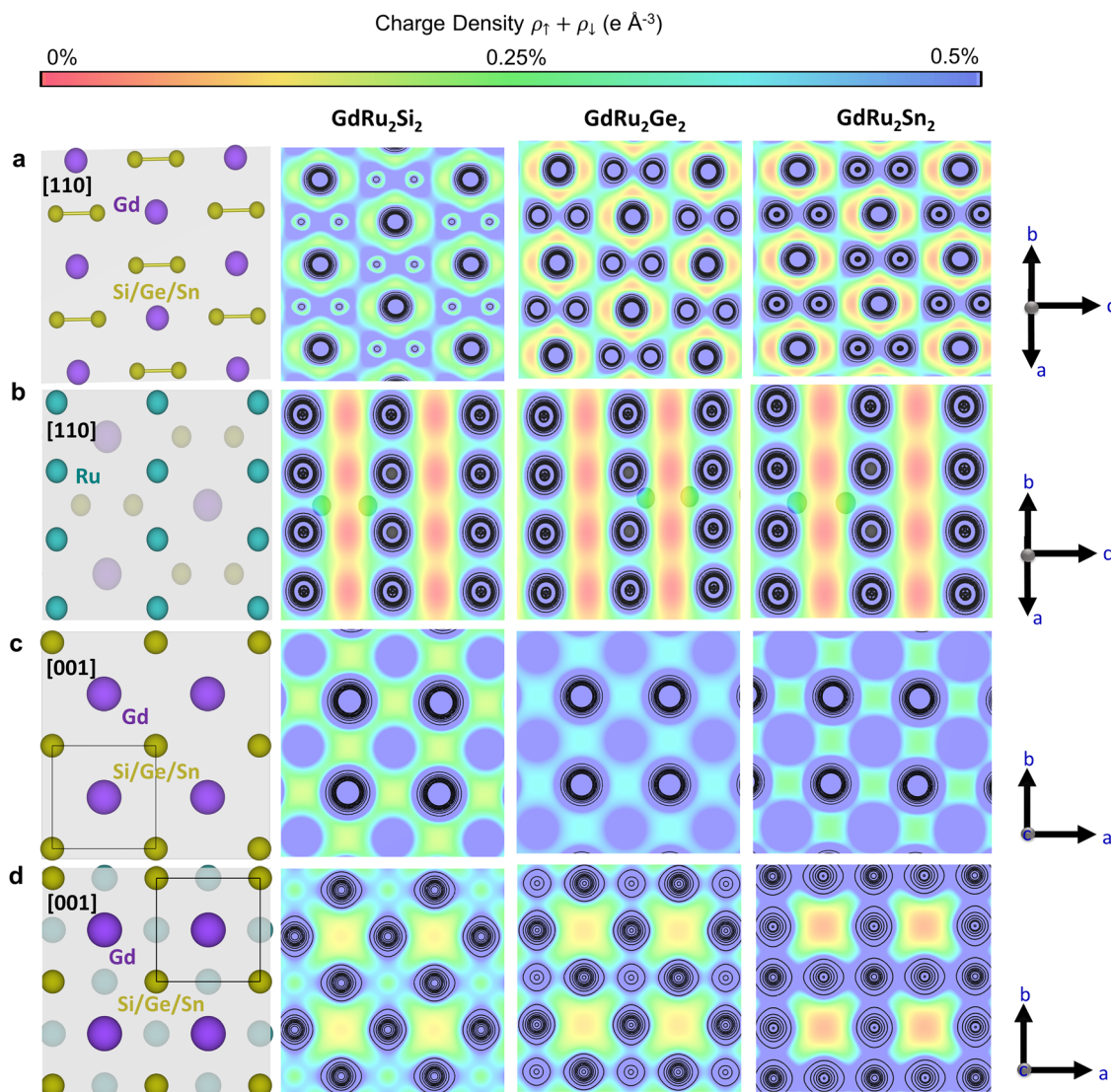
Fig. 6 Charge density map of GdRu$_2$X$_2$ (a) [110] plane cutting through Gd and X atoms, (b) [110] plane cutting through Ru layer, (c) [001] cutting through Gd and X atoms, and (d) [001] plane in between Ru and X atoms. (X = Si, Ge, and Sn).

just below E_F and a flat band segment along the Z–Y$_1$–P–Γ direction, indicating potential topological features (Fig. 2). Overall, this analysis highlights the similarities and differences in the FS characteristics in GdRu$_2$X$_2$. However, these characteristics alone cannot definitively determine the presence or absence of FSN in this system. Therefore, we employed the FermiSurfer software to compute the LRF from the conventional Fermi surface.

FSN and associated divergence in electronic susceptibility, owing to lattice instability, spin density wave modulation, or Friedel oscillations, are understood in several low-dimensional systems through Lindhard susceptibility or the Lindhard response function (LRF).[69,72–74] Such electronic instabilities show up as part of parallel segments in the FS. However, these apparently parallel sections themselves are insufficient to draw conclusive evidence for FSN, as certain geometric and energy conditions are required to obtain FSN. One way to determine a

possible FSN is by calculating the Lindhard susceptibility function $\chi'(q)$ that describes the stability of the electron system. The Lindhard susceptibility function can be written as,

$$\chi'(q) = \sum_{k} \frac{f(\varepsilon_k) - f(\varepsilon_{k+q})}{\varepsilon_k - \varepsilon_{k+q}} \qquad (1)$$

where $f(\varepsilon_k)$ and $f(\varepsilon_{k+q})$ are Fermi–Dirac probability distribution functions related to the occupancy of the states with energy ε_k and ε_{k+q}, respectively.[74] The above equation assumes that the k-dependent matrix element is set to a constant (unity), representing non-interacting electronic susceptibility. Such a function captures the details of the Fermi surface topology and geometrical features; however, the orbital contribution, SOC or multiband effect are captured only if we include the k-dependent matrix element.
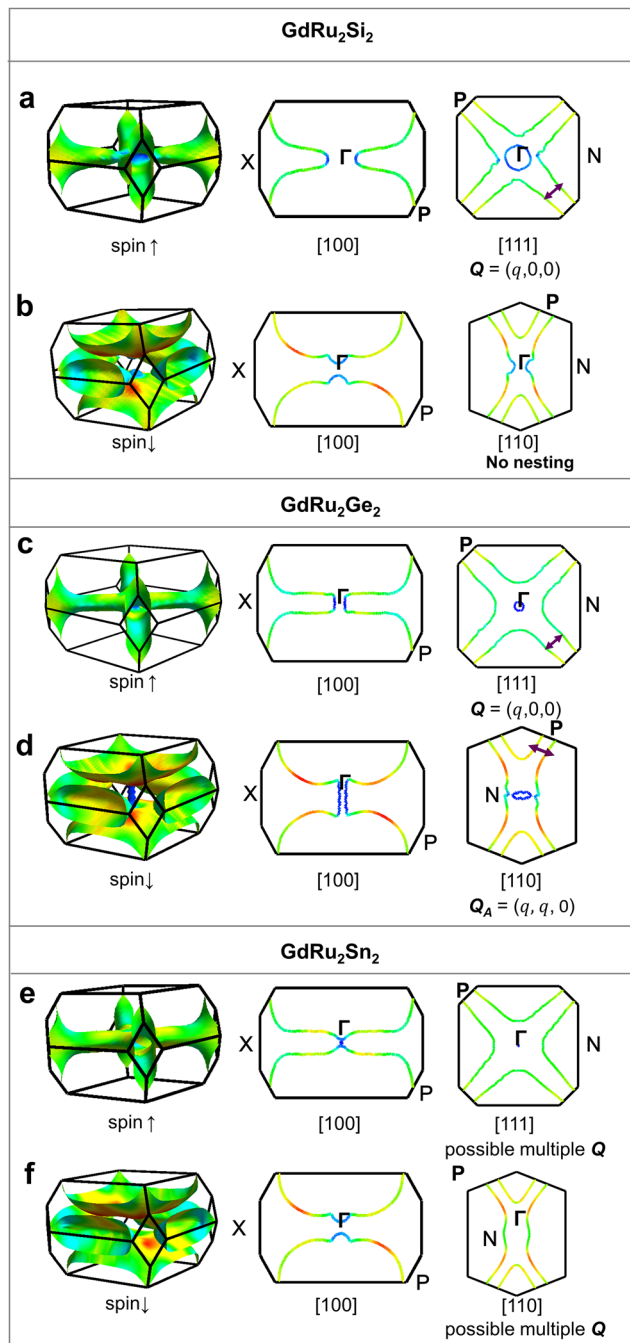
Fig. 7 Fermi surface nesting with respective projections indicating nesting vector for (a)–(b) GdRu$_2$Si$_2$, (c)–(d) GdRu$_2$Ge$_2$, and (e)–(f) GdRu$_2$Sn$_2$, respectively.

The observed parallel regions centered around the X point, perpendicular to the Γ–X direction, suggest a nesting vector $Q_A = (q, 0, 0)$ (Fig. 7a and c), in agreement with previous reports.[40,51] There are diffuse peaks in the Lindhard function at the X point, which is consistent with the observation of the parallel surfaces for both spin-up and spin-down channels for all three compounds. (Fig. 7a and c). In addition, FS and LRF show potential nesting along $Q_B = (q, q, 0)$ r.l.u. and $Q'_B = (-q, -q, 0)$ r.l.u. for GdRu$_2$Ge$_2$ (Fig. S7). This multi-Q FSN

features in GdRu$_2$Ge$_2$ are supported by the work by Yoshimoshi *et al.*, which suggests that the competition of RKKY interactions at inequivalent wavevectors drives the formation of such a rich topological phase.[40] This feature is observed only with Ge and Sn variants, whereas Si shows no nesting along these directions.

For GdRu$_2$Sn$_2$, the Lindhard susceptibility possesses diffuse features for spin-up and doubly degenerate susceptibility peaks and rhombohedral ridge patterns for spin-down (Fig. 8f). These rhombohedral features are also observed in the spin-down channel for GdRu$_2$Ge$_2$. These complex features in the Lindhard response indicate the presence of multiple nesting wavevectors in GdRu$_2$Sn$_2$. This could be attributed to the interactions between the Gd-f/d spins and the [Ru$_2$Sn$_2$] layer, as demonstrated by chemical bonding analysis. Our FSN and LRF analysis capture the interplay between the RKKY interaction and conduction electron density modulation, which is essential for the stabilization of topologically nontrivial spin states in GdRu$_2$X$_2$. The real part of the LRF, governed by eqn (1), can be used to screen geometrical features linked to potential nesting, as observed in a peak or ridge pattern corresponding to electronic instability. However, directly linking nesting to a Peierls instability or density wave ordering must be done by incorporating the k-dependent matrix elements.

Consistent with these FSN assignments, as mentioned above, the k-resolved COHP identifies E_F-proximal antibonding segments along Γ–X and, more sensitively, along P–N, which
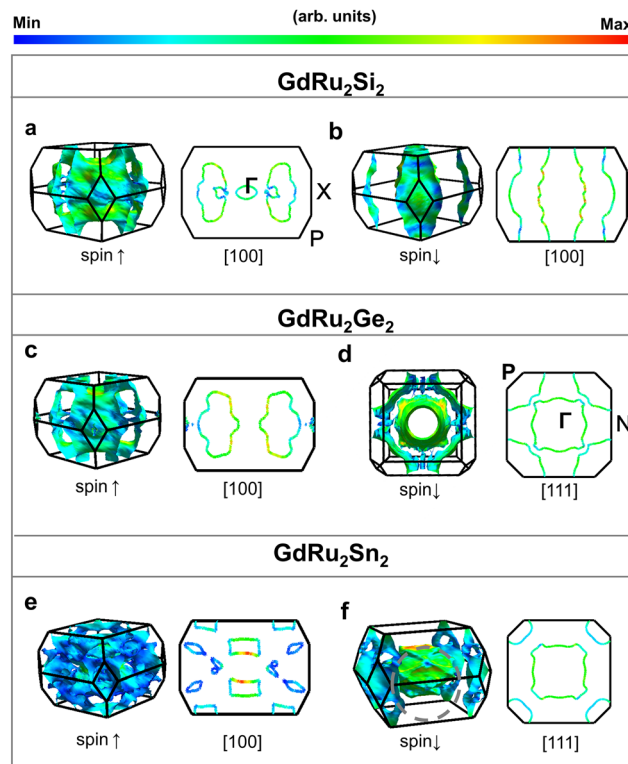

Fig. 8 Lindhard response function with respective projections for (a)–(b) GdRu$_2$Si$_2$ (c)–(d) GdRu$_2$Ge$_2$, and (e)–(f) GdRu$_2$Sn$_2$ respectively. The color bar indicates the real part of $\chi_0(q,0)$ in arbitrary units.

shift toward and through E_F across the series (below E_F in Si, near E_F in Ge, and crossing E_F in Sn). These k-localized antibonding features occur precisely on the band segments that define the parallel FS sheets underlying $Q_A = (q, 0, 0)$ r.l.u and the inequivalent $Q_B = (q, q, 0)$ r.l.u directions. This observation suggests that the occupied antibonding state near E_F enhances susceptibility along those vectors and may facilitate multi-Q behavior in Ge and Sn, where the P–N antibonding is around or crosses E_F, respectively.

3.5.2 Density of energy. The observation of FSN validated by the LRF confirms the presence of electron instability in $GdRu_2X_2$. This argument is further examined by calculating the DOE. The DOE accounts for both interatomic and on-site atomic energy contributions as it integrates the entire electronic band structure with respect to energy (eqn (2)), unlike COHP, which focuses only on interatomic (pair-wise) interactions.[56] Fig. 9 shows the DOEs and the corresponding integrals. Overall, there are strongly destabilizing energy contributions (negative $-DOE$ values), consistent with the electron instability underpinning FSN. The integrated DOE-band energy (E_{band}) for $GdRu_2X_2$ reveals that the chemical substitution of Si by Ge and Sn, separately, increases the overall destabilizing energy (Fig. 9), as suggested by the Ru–Ru and Ru–X COHP curves (Fig. 3). The E_{band} curves of $GdRu_2X_2$ display similar shapes, confirming their resemblance in chemical and crystal structures.

$$E_{band} = \int_{-\infty}^{E_F} DOE(E)\,dE \tag{2}$$

4. Exchange interaction evaluation

In addition to the bonding and DOE analysis, we study the exchange interactions in $GdRu_2X_2$. Building upon our earlier findings,[41] here we performed an energy-mapping analysis, using DFT calculations, as illustrated in Fig. 10.[62,71–73]

The Gd spins form two square sublattices within a unit cell. Our model incorporates the nearest-neighbor exchange interaction J_1 along the a- or b-axis, the exchange interaction J_2 between the Gd square sublattices and the interaction J_3 within the ab-plane along the [110] direction. To accurately simulate an extended solid and avoid artificial interactions between periodic images of atoms, we used a $(2a, 2b, c)$ supercell (containing four formula units) and six different spin-ordered states (Fig. 10). The total spin exchange energy per supercell can be expressed by the following equations:[5]

$$E_1 = E_0 + (-8J_1 + 0J_3 + 0J_2) \times S^2$$
$$E_2 = E_0 + (0J_1 - 16J_3 + 0J_2) \times S^2$$
$$E_3 = E_0 + (0J_1 + 0J_3 - 8J_2) \times S^2$$
$$E_4 = E_0 + (8J_1 - 8J_3 - 0J_2) \times S^2 \tag{3}$$
$$E_5 = E_0 + (8J_1 + 0J_3 + 0J_2) \times S^2$$
$$E_6 = E_0 + (16J_1 - 16J_3 + 0J_2) \times S^2$$

where the E_0 corresponds to the non-magnetic contribution to the total energy, and $S = 7/2$, the spin for Gd^{3+}. From these energies, the exchange interactions per four formula units can be calculated as follows:

$$J_1 = \frac{(E_6 - E_2)}{16S^2}$$
$$J_2 = \frac{(E_1 + E_5 - 2E_3)}{16S^2} \tag{4}$$
$$J_3 = \frac{(E_5 - E_4)}{8S^2}$$

The J-coupling interaction can then be obtained:

As shown in Table 1, J_1 varies from negligible to strong ferromagnetic (FM) when the X site changes from Si to Sn. Meanwhile, J_2 remains unaffected by the X site, which reveals
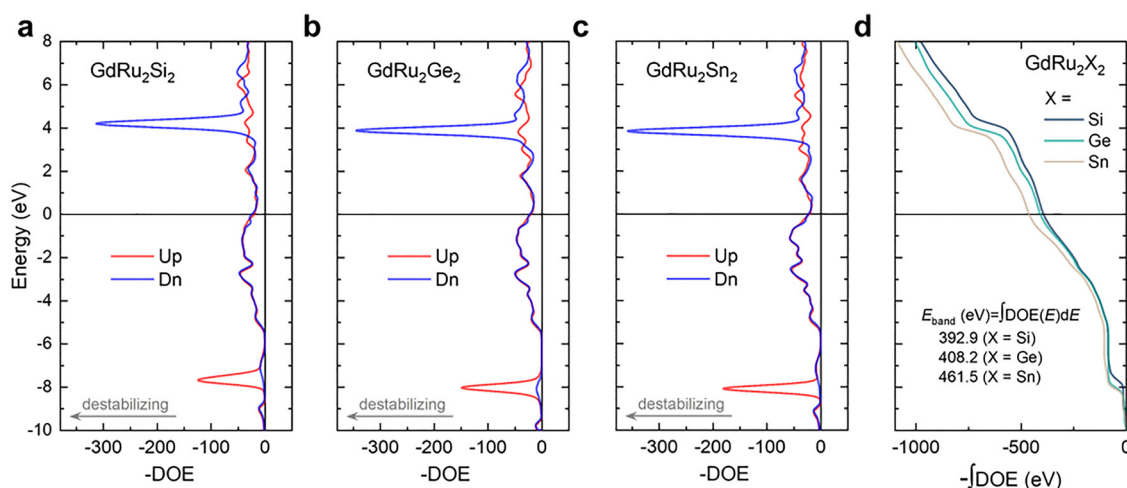

Fig. 9 Density of energy analysis of (a) $GdRu_2Si_2$, (b) $GdRu_2Ge_2$, and (c) $GdRu_2Sn_2$. (d) Comparison of band energy (E_{band}) for $GdRu_2X_2$ where X = Si, Ge and Sn.
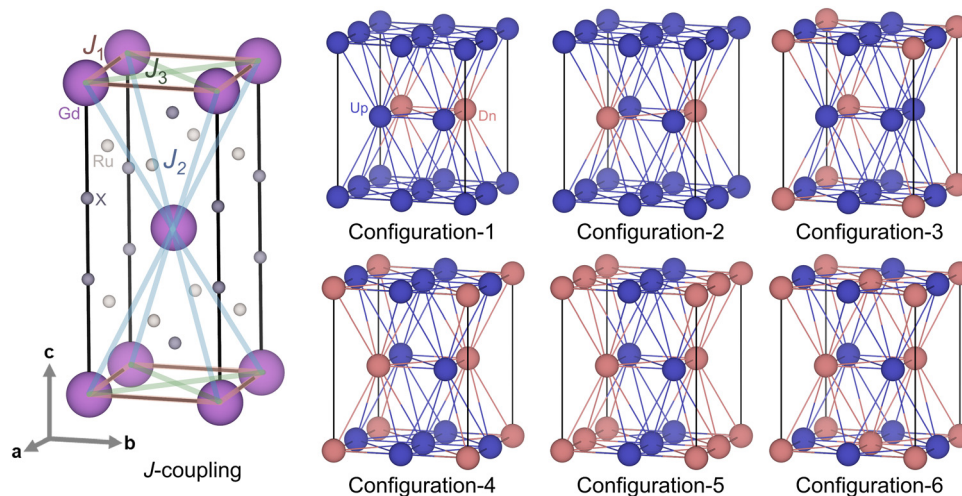
Fig. 10 Representing exchange interactions J_1, J_2 and J_3 between Gd^{3+} atoms within the unit cell and spin-ordered states within the ($2a$, $2b$, c) supercell based on energy mapping method. Pink and blue colors correspond to the spin down and spin up, respectively.

Table 1 Calculated J-coupling constants and an inverse of the mean absolute deviation (MAD^{-1}) for $GdRu_2X_2$ (X = Si, Ge, and Sn)

X Site	$|J_1|$(K)	$|J_2|$ (K)	$|J_3|$ (K)	MAD^{-1}
Si	0.7(2)	153.5(2)	0.5(2)	0.015
Ge	71.1(2)	153.8(2)	2.3(2)	0.019
Sn	76.2(2)	153.0(2)	0.3(2)	0.020

that the shape of the Gd orbitals changes primarily along the a or b axis when Si is replaced by Ge/Sn, suggesting an enhancement of J_1.

To assess the competing strength of these exchange interactions, we calculated the inverse of the mean absolute deviation (MAD^{-1}), which measures the closeness of interaction strengths. As the X site progresses from Si to Ge and Sn, the MAD^{-1} value improves from 0.015 to 0.019 and 0.020, respectively. This increase in the appreciable, competing FM and AFM interactions in the Gd square lattice (the ab-plane) as a function of X follows similar trends in enhanced electronic instability and destabilizing energy E_{band}. Competing FM and

AFM interactions bear a resemblance to those in other skyrmion hosts.

For further insight into long-range RKKY exchange interactions within $GdRu_2Ge_2$, additional exchange interaction calculations were performed based on the magnetic force theorem using the LKAG scheme. Magnetic exchange constants (J_{ij}) between Gd moments as a function of scaled distance (R/a) are shown in Fig. 11(a). We observed predominantly FM interactions (positive J_{ij}) for (R/a) < 2; however, oscillatory behavior is seen up to (R/a) = 7, indicating long-range RKKY J_{ij} interaction. The strongest interaction is identified as the second-neighbor (interlayer) coupling J_2, corresponding to the body-diagonal direction [111]. Since J_8 ((R/a) = c) also shows a strong ferromagnetic interaction, the interplane exchange (J_2, J_8) is stronger than the basal-plane interactions J_1 and J_3. The competition between intra- and interlayer exchange frustration suggests the presence of non-collinear magnetic ordering in $GdRu_2Ge_2$. To examine whether the system has spin density wave modulation, we performed a lattice Fourier transform of the real-space exchange constants and estimated $J(q)$, with q
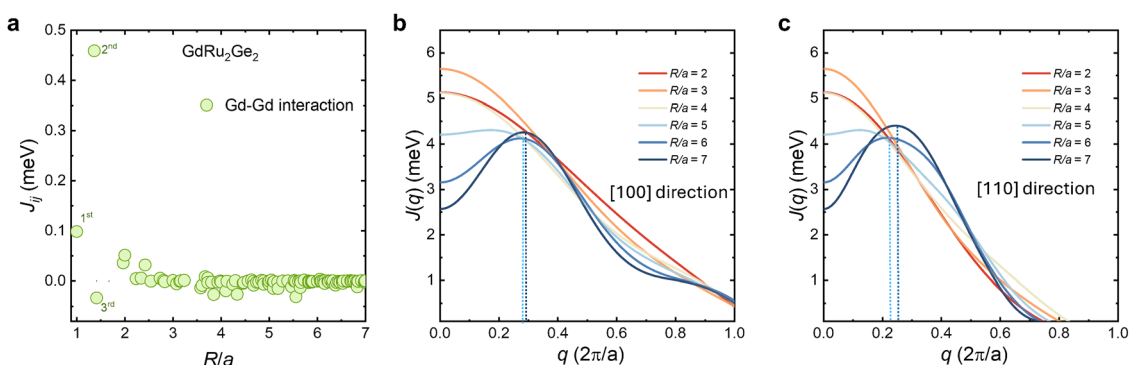

Fig. 11 Exchange interaction calculations based on magnetic force theorem (a) Gd−Gd exchange interactions as a function of reciprocal lattice distance $J_{ij}(R)$, R − lattice translational vector, a − lattice constant and (R/a) − cluster radius, (b) and (c) reciprocal space exchange interaction function $J(q)$ along [100] and [110] directions respectively.

expressed in units of $2\pi/a$ (Fig. 11b). For cluster radii smaller than 4, FM interaction is stabilized, but above this radius we observed a stable peak with an amplitude of about 4 meV, located at $Q_A = (0.3,0,0)$ r.l.u. along Γ–X direction. This SDW modulation was observed experimentally in both $GdRu_2Ge_2$ and $GdRu_2Si_2$.[41,48,74] The Fourier transform of J_{ij} along the Γ–M direction [110] also shows a peak at $Q_B = (0.25,0.25,0)$ r.l.u. with an amplitude of 4.5 meV, indicating that the system favors a multi-Q state where the modulations along [100] and [110] coexist (Fig. 11b and c).

We propose a correlation between E_{band} and the temperature and magnetic field conditions at which skyrmions emerge (Fig. 12). For the Si and Ge materials, the conditions for skyrmion formation have been experimentally proven. Our attempts to create the Sn version have not been fruitful yet, possibly due to its highest electron instability and thermodynamically unfavorable formation energy among the series. $GdRu_2Sn_2$ exhibits 72 meV per atom above the convex hull and is predicted to decompose into $GdSn_2 + 2Ru$ (Fig. S1b). Unconventional synthesis approaches, such as ion exchange or high-pressure synthesis, may be required to access this metastable phase. While we are making additional efforts to create $GdRu_2Sn_2$, we predict that this phase hosts skyrmions at a higher temperature and a lower field than its siblings, attributable to its highest destabilizing energy E_{band}. This prediction can be justified by the DOE formalism, which fundamentally paints the entire energetic picture.

Taken together, we propose a trend: the more destabilizing energy E_{band} and the more competing FM and AFM interactions in the Gd square lattice, the more accessible skyrmion formation becomes (higher temperatures and lower fields) (Fig. 12). This suggestion demonstrates that destabilizing energy contributions and competing interaction strengths can serve as indicators for predicting and realizing the emergence of skyrmions. While the suggested trend may prove useful, it warrants rigorous experimental evidence for the Sn material.

5. Conclusions

Developing skyrmion materials for spintronics requires a comprehensive understanding of the chemical origins that facilitate a system undergoing a phase transition under a given condition to form topologically distinct spin phases. Our results provide a new pathway toward understanding and developing centrosymmetric magnetic metals that host skyrmions, rooted in chemical concepts in solids. We study the impact of X-p (Si-3p/Ge-4p/Sn-5p) orbitals on the skyrmion evolution in $GdRu_2X_2$. The chemical bonding analysis reveals that increased interactions occur between the Gd-4f localized electrons and the $[Ru_2X_2]$ conduction layer as X changes from Si-3p to Ge-4p and Sn-5p (resulting in more extended orbitals). The realization of FSN indicates the electron instability in $GdRu_2X_2$. In this analysis, an FSN vector $[Q_A = (q, 0, 0)]$ r.l.u. and two inequivalent FSN vectors $[Q_A = (q, 0, 0); Q_B = (q, q, 0)]$ r.l.u. are extracted for the Si and Ge compounds, respectively. For the Sn material, multiple FSN vectors are suggested. The competition between RKKY interactions at different wavevectors, stemming from FSN along several directions, can work in favor of skyrmion formation in centrosymmetric magnetic metals. The DOE analysis complements COHP in that it captures the significance of both interatomic and atomic energetic contributions for electron (in)stability. We propose that the more destabilizing energy and the stronger competing interaction, the more accessible conditions are for skyrmions to emerge (at higher temperatures and lower fields). Ongoing experimental studies on the Sn compound will help verify this proposed trend. Overall, our work provides a new framework for approaching skyrmion materials research from chemical bonding and electronic instability perspectives, while inviting other studies to dissect the multifaceted aspects of the emergence of topologically nontrivial states of matter for high-density memory and logic architectures.

Author contributions

The manuscript was written through the contributions of all authors. All authors have given approval to the final version of the manuscript.

Conflicts of interest

There are no conflicts to declare.

Abbreviations

RKKY	Ruderman–Kittel–Kasuya–Yosida (exchange interaction)
FSN	Fermi surface nesting

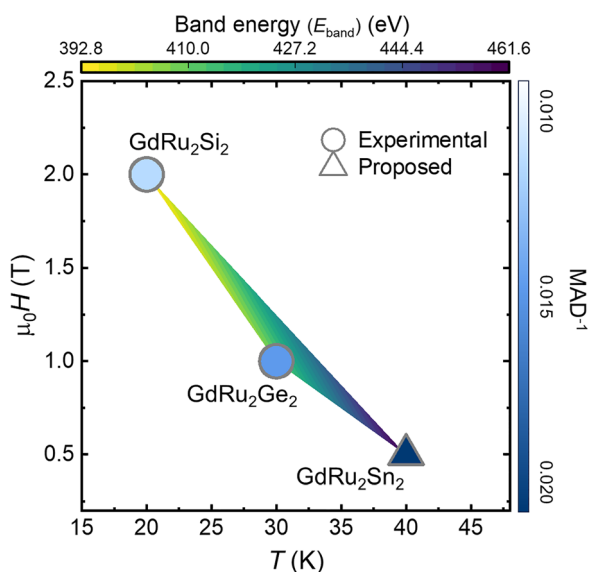**Fig. 12** Correlation between skyrmion formation T, and $\mu_0 H$ with band energy (E_{band}) for $GdRu_2X_2$ (X = Si, Ge, and Sn), with the blue color filling indicate the MAD^{-1}.

DFT	Density functional theory
GGA	Generalized gradient approximation
PAW	Projector augmented wave
LCAO	Linear combination of atomic orbitals
LOBSTER	Local orbital basis suite towards electronic-structure reconstruction
COHP	Crystal orbital Hamilton population
k-COHP	k-Space resolved crystal orbital Hamilton population
COBI	Crystal orbital bond index
ICOHP	Integrated crystal orbital Hamilton population
ICOBI	Integrated crystal orbital bond index
MO	Molecular orbital
DOE	Density of energy
LRF	Lindhard response function
FS	Fermi surface
FM/AFM	Ferromagnetic/antiferromagnetic
MAD	Mean absolute deviation

Data availability

The data supporting this article have been included as part of the supplementary information (SI). Supplementary information: additional data analysis, tables, figures, including COBI, Fermi surface. See DOI: **https://doi.org/10.1039/d5tc02333e**.

Acknowledgements

References

1 X. Gui, R. A. Klein, C. M. Brown and W. Xie, Chemical Bonding Governs Complex Magnetism in MnPt₅P, *Inorg. Chem.*, 2020, **60**, 87–96.

2 T. Berry, *et al.*, Bonding and Suppression of a Magnetic Phase Transition in EuMn₂P₂, *J. Am. Chem. Soc.*, 2023, **145**, 4527–4533.

3 S. M. Amtry, *et al.*, Chemical Design of Spin Frustration to Realize Topological Spin Glasses, *J. Am. Chem. Soc.*, 2024, **146**, 29040–29052.

4 C. J. Pollak, *et al.*, Chemical Bonding Induces One-Dimensional Physics in Bulk Crystal BiIr₄Se₈, *J. Am. Chem. Soc.*, 2024, **146**, 6784–6795.

5 X. Huai, *et al.*, Noncentrosymmetric Triangular Magnet CaMnTeO₆: Strong Quantum Fluctuations and Role of s⁰ versus s² Electronic States in Competing Exchange Interactions, *Adv. Mater.*, 2024, **36**, 2313763.

6 K. D. Shumilov, A. J. Jenkins, H. S. La Pierre, B. Vlaisavljevich and X. Li, Overdestabilization vs. Overstabilization in the Theoretical Analysis of f-Orbital Covalency, *J. Am. Chem. Soc.*, 2024, **146**, 12030–12039.

7 H. Li, *et al.*, Discovery of conjoined charge density waves in the kagome superconductor CsV₃Sb₅, *Nat. Commun.*, 2022, **13**, 6348.

8 B. Zhang, H. Tan, B. Yan, C. Xu and H. Xiang, Atomistic Origin of Diverse Charge Density Wave States in CsV₃Sb₅, *Phys. Rev. Lett.*, 2024, **132**, 096101.

9 Y. Kurtulus, M. Gillelßen and R. Dronskowski, Electronic structure, chemical bonding, and finite-temperature magnetic properties of full Heusler alloys, *J. Comput. Chem.*, 2006, **27**, 90–102.

10 M. Yu, *et al.*, Tunable eg orbital occupancy in Heusler compounds for oxygen evolution reaction, *Angew. Chem., Int. Ed.*, 2021, **60**, 5800–5805.

11 A. Neubauer, *et al.*, Topological Hall effect in the A phase of MnSi, *Phys. Rev. Lett.*, 2009, **102**, 186602.

12 X. Zhang, *et al.*, Skyrmion-electronics: writing, deleting, reading and processing magnetic skyrmions toward spintronic applications, *J. Phys.: Condens. Matter*, 2020, **32**, 143001.

13 Y. Tokura and N. Kanazawa, Magnetic skyrmion materials, *Chem. Rev.*, 2020, **121**, 2857–2897.

14 S. Roychowdhury, *et al.*, Giant Room-Temperature Topological Hall Effect in a Square-Net Ferromagnet LaMn₂Ge₂, *Adv. Mater.*, 2024, **36**, 2305916.

15 B. Chen, *et al.*, Spintronic devices for high-density memory and neuromorphic computing–A review, *Mater. Today*, 2023, **70**, 193–217.

16 C. Pfleiderer and A. Rosch, Single skyrmions spotted, *Nature*, 2010, **465**, 880–881.

17 N. Tang, *et al.*, Skyrmion-Excited Spin-Wave Fractal Networks, *Adv. Mater.*, 2023, **35**, 2300416.

18 C. Felser, Skyrmions, *Angew. Chem., Int. Ed.*, 2013, **52**, 1631–1634.

19 K. Wang, V. Bheemarasetty, J. Duan, S. Zhou and G. Xiao, Fundamental physics and applications of skyrmions: A review, *J. Magn. Magn. Mater.*, 2022, **563**, 169905.

20 N. Kumar, S. N. Guin, K. Manna, C. Shekhar and C. Felser, Topological quantum materials from the viewpoint of chemistry, *Chem. Rev.*, 2020, **121**, 2780–2815.

21 S. Parkin and S.-H. Yang, Memory on the racetrack, *Nat. Nanotechnol.*, 2015, **10**, 195–198.

22 X. Huai and T. T. Tran, Design principles for noncentrosymmetric materials, *Annu. Rev. Mater. Res.*, 2023, **53**, 253–274.

23 E. E. Oyeka, *et al.*, Potential skyrmion host $Fe(IO_3)_3$: connecting stereoactive lone-pair electron effects to the Dzyaloshinskii-Moriya interaction, *Chem. Mater.*, 2021, **33**, 4661–4671.

24 N. Kanazawa, S. Seki and Y. Tokura, Noncentrosymmetric magnets hosting magnetic skyrmions, *Adv. Mater.*, 2017, **29**, 1603227.

25 C. Zhang, *et al.*, Above-room-temperature chiral skyrmion lattice and Dzyaloshinskii–Moriya interaction in a van der Waals ferromagnet $Fe_{3−x}GaTe_2$, *Nat. Commun.*, 2024, **15**, 4472.

26 Y. Zhang, *et al.*, Stable skyrmion bundles at room temperature and zero magnetic field in a chiral magnet, *Nat. Commun.*, 2024, **15**, 3391.

27 D. Singh, *et al.*, Transition between distinct hybrid skyrmion textures through their hexagonal-to-square crystal transformation in a polar magnet, *Nat. Commun.*, 2023, **14**, 8050.

28 I. Kézsmárki, *et al.*, Néel-type skyrmion lattice with confined orientation in the polar magnetic semiconductor GaV_4S_8, *Nat. Mater.*, 2015, **14**, 1116–1122.

29 A. Chacon, *et al.*, Observation of two independent skyrmion phases in a chiral magnetic material, *Nat. Phys.*, 2018, **14**, 936–941.

30 S. Mühlbauer, *et al.*, Skyrmion lattice in a chiral magnet, *Science*, 2009, **323**, 915–919.

31 T. Adams, *et al.*, Long-wavelength helimagnetic order and skyrmion lattice phase in Cu_2OSeO_3, *Phys. Rev. Lett.*, 2012, **108**, 237204.

32 T. Kurumaji, *et al.*, Néel-type skyrmion lattice in the tetragonal polar magnet $VOSe_2O_5$, *Phys. Rev. Lett.*, 2017, **119**, 237201.

33 B. W. Casas, *et al.*, Coexistence of merons with skyrmions in the centrosymmetric van der Waals ferromagnet Fe5–xGeTe2, *Adv. Mater.*, 2023, **35**, 2212087.

34 D.-H. Kim, *et al.*, Bulk Dzyaloshinskii–Moriya interaction in amorphous ferrimagnetic alloys, *Nat. Mater.*, 2019, **18**, 685–690.

35 S. Ishiwata, *et al.*, Emergent topological spin structures in the centrosymmetric cubic perovskite $SrFeO_3$, *Phys. Rev. B*, 2020, **101**, 134406.

36 T. Kurumaji, *et al.*, Skyrmion lattice with a giant topological Hall effect in a frustrated triangular-lattice magnet, *Science*, 2019, **365**, 914–918.

37 J. M. Moya, *et al.*, Incommensurate magnetic orders and topological Hall effect in the square-net centrosymmetric $EuGa_2Al_2$ system, *Phys. Rev. Mater.*, 2022, **6**, 074201.

38 Y. Yasui, *et al.*, Imaging the coupling between itinerant electrons and localised moments in the centrosymmetric skyrmion magnet $GdRu_2Si_2$, *Nat. Commun.*, 2020, **11**, 5925.

39 Y. Zhou, S. Li, X. Liang and Y. Zhou, Topological spin textures: Basic physics and devices, *Adv. Mater.*, 2025, **37**, 2312935.

40 H. Yoshimochi, *et al.*, Multistep topological transitions among meron and skyrmion crystals in a centrosymmetric magnet, *Nat. Phys.*, 2024, **20**, 1–8.

41 D. N. Rathnaweera, X. Huai, K. Ramesh Kumar, M. J. Winiarski, T. Klimczuk and T. T. Tran, Atomically Modulating Competing Exchange Interactions in Centrosymmetric Skyrmion Hosts $GdRu_2X_2$ (X = Si, Ge) (2025), **https://arxiv.org/abs/2502.21169**.

42 N. D. Khanh, *et al.*, Nanometric square skyrmion lattice in a centrosymmetric tetragonal magnet, *Nat. Nanotechnol.*, 2020, **15**, 444–449.

43 L. Gries, *et al.*, Uniaxial pressure effects, phase diagram, and tricritical point in the centrosymmetric skyrmion lattice magnet $GdRu_2Si_2$, *Phys. Rev. B*, 2025, **111**, 064419.

44 S. Gupta, *et al.*, Skyrmion phase in polycrystalline $GdRu_2Si_2$ revealed by magnetic susceptibility, topological Hall effect, and Shubnikov–de Haas-like quantum oscillations, *Phys. Rev. B*, 2025, **111**, 144405.

45 T. Nomoto, T. Koretsune and R. Arita, Formation mechanism of the helical Q structure in Gd-based skyrmion materials, *Phys. Rev. Lett.*, 2020, **125**, 117204.

46 T. Nomoto and R. Arita, Ab initio exploration of short-pitch skyrmion materials: Role of orbital frustration, *J. Appl. Phys.*, 2023, **133**, 150901.

47 S. Siebeneichler, A. Ovchinnikov, D. Sheptyakov and A.-V. Mudring, Making a Hedgehog Spin-Vortex State Possible: Geometric Frustration on a Square Lattice, *Chem. Mater.*, 2024, **36**, 3546–3554.

48 G. D. A. Wood, *et al.*, Double-Q ground state with topological charge stripes in the centrosymmetric skyrmion candidate $GdRu_2Si_2$, *Phys. Rev. B*, 2023, **107**, L180402.

49 N. D. Khanh, *et al.*, Zoology of Multiple-Q Spin Textures in a Centrosymmetric Tetragonal Magnet with Itinerant Electrons, *Adv. Sci.*, 2022, **9**, 2105452.

50 N. Matsuyama, *et al.*, Quantum oscillations in the centrosymmetric skyrmion-hosting magnet $GdRu_2Si_2$, *Phys. Rev. B*, 2023, **107**, 104421.

51 S. V. Eremeev, *et al.*, Insight into the electronic structure of the centrosymmetric skyrmion magnet $GdRu_2Si_2$, *Nanoscale Adv.*, 2023, **5**, 6678–6687.

52 S. Maintz, V. L. Deringer, A. L. Tchougréeff and R. Dronskowski, LOBSTER: A tool to extract chemical bonding from plane-wave based DFT, *J. Comput. Chem.*, 2016, **37**, 1030–1035.

53 V. L. Deringer, A. L. Tchougréeff and R. Dronskowski, Crystal orbital Hamilton population (COHP) analysis as projected from plane-wave basis sets, *J. Phys. Chem. A*, 2011, **115**, 5461–5466.

54 X. Sun, *et al.*, Achieving band convergence by tuning the bonding ionicity in n-type Mg_3Sb_2, *J. Comput. Chem.*, 2019, **40**, 1693–1700.

55 P. C. Müller, C. Ertural, J. Hempelmann and R. Dronskowski, Crystal orbital bond index: Covalent bond orders in solids, *J. Phys. Chem. C*, 2021, **125**, 7959–7970.

56 M. Küpers, *et al.*, Unexpected Ge–Ge contacts in the two-dimensional Ge_4Se_3Te Phase and analysis of their chemical cause with the density of energy (DOE) function, *Angew. Chem., Int. Ed.*, 2017, **56**, 10204–10208.

57 Y. Wang, P. C. Müller, D. Hemker and R. Dronskowski, LOPOSTER: A Cascading Postprocessor for LOBSTER, *J. Comput. Chem.*, 2025, **46**, e70167.

58 M. Kawamura, FermiSurfer: Fermi-surface viewer providing multiple representation schemes, *Comput. Phys. Commun.*, 2019, **239**, 197–203.

59 H. Ebert, D. Koedderitzsch and J. Minar, Calculating condensed matter properties using the KKR-Green's function method—recent developments and applications, *Rep. Prog. Phys.*, 2011, **74**, 096501.

60 S. H. Vosko, L. Wilk and M. Nusair, Accurate spin-dependent electron liquid correlation energies for local spin density calculations: a critical analysis, *Can. J. Phys.*, 1980, **58**, 1200–1211.

61 A. I. Liechtenstein, M. Katsnelson, V. Antropov and V. Gubanov, Local spin density functional approach to the theory of exchange interactions in ferromagnetic metals and alloys, *J. Magn. Magn. Mater.*, 1987, **67**, 65–74.

62 P. Giannozzi, *et al.*, QUANTUM ESPRESSO: a modular and open-source software project for quantum simulations of materials, *J. Phys.: Condens. Matter*, 2009, **21**, 395502.

63 S. Maintz, V. L. Deringer, A. L. Tchougréeff and R. Dronskowski, (Wiley Online Library, 2016).

64 R. Nelson, *et al.*, LOBSTER: Local orbital projections, atomic charges, and chemical-bonding analysis from projector-augmented-wave-based density-functional theory, *J. Comput. Chem.*, 2020, **41**, 1931–1940.

65 R. Dronskowski and P. E. Blöchl, Crystal orbital Hamilton populations (COHP): energy-resolved visualization of chemical bonding in solids based on density-functional calculations, *J. Phys. Chem.*, 1993, **97**, 8617–8624.

66 S. Maintz, V. L. Deringer, A. L. Tchougréeff and R. Dronskowski, Analytic projection from plane-wave and PAW wavefunctions and application to chemical-bonding analysis in solids, *J. Comput. Chem.*, 2013, **34**, 2557–2567.

67 R. Dronskowski, *Computational chemistry of solid state materials: a guide for materials scientists, chemists, physicists and others*, John Wiley & Sons, 2008, vol. 146.

68 P. C. Muller, L. S. Reitz, D. Hemker and R. Dronskowski, Orbital-Based Bonding Analysis in Solids, *Chem. Sci.*, 2025, **16**, 12212–12226.

69 P. C. Müller, N. Schmit, L. Sann, S. Steinberg and R. Dronskowski, Fragment Orbitals Extracted from First-Principles Plane-Wave Calculations, *Inorg. Chem.*, 2024, **63**, 20161–20172.

70 G. A. Landrum, R. Dronskowski, R. Niewa and F. J. DiSalvo, Electronic structure and bonding in cerium (nitride) compounds: Trivalent versus tetravalent cerium, *Chem. – Eur. J.*, 1999, **5**, 515–522.

71 M.-H. Whangbo, H.-J. Koo and D. Dai, Spin exchange interactions and magnetic structures of extended magnetic solids with localized spins: theoretical descriptions on formal, quantitative and qualitative levels, *J. Solid State Chem.*, 2003, **176**, 417–481.

72 H. Xiang, C. Lee, H.-J. Koo, X. Gong and M.-H. Whangbo, Magnetic properties and energy-mapping analysis, *Dalton Trans.*, 2013, **42**, 823–853.

73 E. A. Zvereva, *et al.*, Hidden magnetic order in the triangular-lattice magnet Li_2MnTeO_6, *Phys. Rev. B*, 2020, **102**, 094433.

74 S. Sarkar, *et al.*, Unveiling Mysteries of GdRu2Si2: 3D Magnetism in a layered like Magnet, *arXiv*, 2024, preprint, arXiv:2409.06736.